

pubs.acs.org/cm Article

# Heterocyclic Modification Leading to Luminescent 0D Metal Organochalcogenide with Stable X-ray Scintillating Properties

Rattapon Khamlue,<sup>∇</sup> Tomoaki Sakurada,<sup>∇</sup> Yeongsu Cho, Woo Seok Lee, Pimpan Leangtanom, Michael G. Taylor, Worakit Naewthong, Pongsakun Sripetch, Busayakorn Na Ranong, Tossawat Autila, Thiti Rungseesumran, Jakrapong Kaewkhao, Taweesak Sudyoadsuk, Atcha Kopwitthaya, Peter Müller, Vinich Promarak, Heather J. Kulik, William A. Tisdale,\* and Watcharaphol Paritmongkol\*



Cite This: Chem. Mater. 2024, 36, 5238-5249



ACCESS

III Metrics & More

Article Recommendations

Supporting Information

ABSTRACT: Metal organochalcogenides (MOCs) are an emerging class of luminescent hybrid organic—inorganic semiconductors, whose structures and properties can be tuned by organic functionalization and substitutions of their metal and chalcogen elements. Herein, we present a new design strategy by heterocyclic modification, resulting in the transformation of prototypical two-dimensional (2D) silver phenylselenide (AgSePh) to a zero-dimensional (0D) silver pyridinylselenide (AgSePy) via the formation of Ag–N bonds. At room temperature, AgSePy shows strong and broad orange photoluminescence (PL;  $\lambda_{\text{max}}$  = 636 nm, full-width-at-half-maximum = 111 nm, quantum yield = 64%) with a large 259 nm Stoke's shift and a 3.4  $\mu$ s lifetime. Using steady-state and time-



resolved PL spectroscopy under varying temperature and oxygen conditions, we found AgSePy to exhibit air-stable luminescence and maintain a high PL quantum yield and a single exponential PL lifetime down to 4 K. Furthermore, AgSePy shows excellent thermal stability up to  $\sim$ 250 °C and chemical stability against polar, nonpolar, and aqueous solvents at pH 3–14. Density functional theory calculations further confirm the 0D electronic structure. Finally, we successfully demonstrated the performance of AgSePy as an X-ray scintillator with an estimated light yield of  $\sim$ 8,000 phe/MeV and a spatial resolution down to 0.080  $\pm$  0.005 mm. Overall, this work provides a novel tactic to modify the structures and properties of MOCs, highlighting their structural richness and structure—property relationship, and introduces their new use as X-ray scintillators, encouraging further development in radiation detection and medical imaging.

# 1. INTRODUCTION

Metal organochalcogenides (MOCs)<sup>1,2</sup> are an emerging class of hybrid organic—inorganic materials with metal and organochalcogenide units linked by covalent metal—chalcogen bonds. They typically exhibit luminescent properties and excellent chemical stability<sup>1</sup> and can be synthesized at low temperatures in various forms including powders,<sup>3–5</sup> microcrystals,<sup>6–8</sup> single crystals,<sup>8,9</sup> and thin films.<sup>10–13</sup> While the research on this materials class was focused mainly on MOCs of coinage metals with  $[M(ER)]_n$  formula,<sup>1</sup> where M = Cu(I), Ag(I), and Au(I); E = S, Se, Te; and R is an organic hydrocarbon, the concept of MOCs has recently been extended to other metals including indium, lead, and tin.<sup>14,15</sup>

Due to their rich structural flexibility, MOCs' properties and structures have been tailored by various methods. These include introduction of organic functional groups<sup>16–21</sup> and substitution of inorganic elements, <sup>17,19,22</sup> leading to strong and robust luminescence of multiple MOC members and their potential uses in various applications. For example, *para*-substitution of the phenylsulfide ligand with carboxylic groups (–COOH) transforms a nonemissive copper phenylsulfide, [Cu(SPh)]<sub>n</sub>, with a one-dimensional (1D) polymeric structure

into a luminescent copper 4-carboxyphenylsulfide,  $[Cu(p-SPhCOOH)]_n$ , having a two-dimensional (2D), layered structure. The luminescence of the modified  $[Cu(p-SPhCOOH)]_n$  also changes colors with temperature, enabling its use as a thermochromic sensor. Similarly, fluorination of blue-emitting 2D silver phenylselenide (AgSePh) at the ortho positions results in the formation of yellow-emissive 1D silver 2,6-difluorophenylselenide (AgSePh-F<sub>2</sub>(2,6)). In another example, insertion of an alkyl spacer between a chalcogen and a phenyl ring reduces the glass transition temperature with increasing spacer length from 1D gold(I) phenylsulfide,  $[Au(SPh)]_n$ , to gold(I) phenmethylsulfide  $[Au(SMePh)]_n$  and gold(I) phenethylsulfide  $[Au(SEtPh)]_n$ . After the transition,  $[Au(SEtPh)]_n$  also shows a marked improvement

Received: March 6, 2024 Revised: May 1, 2024 Accepted: May 2, 2024 Published: May 7, 2024





in photoluminescence quantum yield (PLQY) from 2% to 71%, opening up a possibility as a candidate for a phase-change random access memory application. Moreover, Cu substitution shifts the luminescent color from green in silver 4-carboxyphenylsulfide,  $[Ag(\textit{p-SPhCOOH})]_n$ , to red in  $[Ag_{0.85}Cu_{0.15}(\textit{p-SPhCOOH})]_n^{22}$  and replacing S by Se and Te changes the optical bandgap of silver phenylsulfide (AgSPh) from 380 nm to 467 nm and 620 nm, respectively.  $^{21,24,25}$ 

In this work, we present an alternative design strategy to tune the properties of MOCs by heterocyclic modification. Introducing a pyridine ligand, we synthesized silver pyridinylselenide (AgSePy) showing strong and robust orange luminescence, as well as excellent thermal and chemical stability across various solvents and pHs. Compared to AgSePh, a prototypical member of AgSe MOCs, 26 and its derivatives which tend to adopt layered two-dimensional (2D) structures,<sup>27</sup> this modification strategy leads to structural transformation into a zero-dimensional (0D) complex of the [AgSePy]<sub>6</sub> unit. Detailed investigation by means of photoluminescence excitation (PLE) spectroscopy and temperaturedependent and time-resolved photoluminescence (PL) spectroscopy under controlled environments was conducted to reveal the origin of its strong luminescence, and density functional theory (DFT) calculations were performed to confirm its 0D electronic structure. Additionally, due to its robust and strong luminescence coupled with its outstanding thermal and chemical stability, we investigated its potential use as an X-ray scintillator film and found multiple characteristics competing with a commercial reference.

## 2. EXPERIMENTAL SECTION

- **2.1. Chemicals.** All starting chemicals were obtained from suppliers (TCI, Sigma-Aldrich, Merck, Qrec, DAEJUNG, and Fisher Scientific) and used without further purification.
- **2.2. Synthesis.** 2.2.1. Synthesis of 1,2-Di(pyridin-2-yl) Diselenide  $(Py_2Se_2)$ . To a suspension of elemental selenium (1.58 g, 20 mmol) in deionized water (20 mL) degassed by N2 gas bubbling at 0 °C for 30 min, an aqueous solution of sodium borohydride (0.76 g, 20 mmol, 4 mL) was added dropwise and stirred under N2 flow for 30 min to form a brown solution of sodium diselenide (Na<sub>2</sub>Se<sub>2</sub>). Subsequently, 2-bromopyridine (3.0 g, 19 mmol) was added in one portion, and the solution was refluxed at 110 °C for 4 h. After the reaction was complete, the hot reaction mixture was filtered and cooled in a refrigerator overnight to obtain yellow solids. The yellow solids were collected by suction filtration and redissolved in chloroform. This organic solution was washed with a saturated sodium chloride (NaCl) aqueous solution and dried with sodium sulfate (Na<sub>2</sub>SO<sub>4</sub>). After that, the solvent was removed by rotary evaporation, and the resulting crude product was recrystallized using a 1:3 chloroform/hexane mixture, yielding 1,2-di(pyridin-2-yl) diselenide (Py<sub>2</sub>Se<sub>2</sub>) as yellow needle crystals (2.452 g, 27% yield).  $^{1}$ H NMR (600 MHz, CDCl<sub>3</sub>)  $\delta$ 8.46 (dd, *J* = 4.9, 1.9 Hz, 2H), 7.80 (d, *J* = 8.0 Hz, 2H), 7.54 (td, *J* = 7.8, 1.9 Hz, 2H), 7.08 (dd, J = 7.8, 4.9 Hz, 2H). <sup>13</sup>C NMR (151 MHz, CDCl<sub>3</sub>)  $\delta$  154.41, 149.54, 137.57, 123.67, 121.27. <sup>77</sup>Se NMR (115 MHz, CDCl<sub>3</sub>)  $\delta$  447.99 ppm. HRMS-APCI (m/z): [MH]<sup>+</sup> calcd for C<sub>10</sub>H<sub>8</sub>N<sub>2</sub>Se<sub>2</sub>: 315.9018, found: 316.9284.
- 2.2.2. Synthesis of Silver Pyridinylselenolate (AgSePy) Crystals by a Single-Phase Reaction. Crystals of AgSePy were prepared by mixing equal volumes of a 50 mM solution of Py<sub>2</sub>Se<sub>2</sub> in toluene and a 50 mM solution of AgNO<sub>3</sub> in propylamine (PrNH<sub>2</sub>) at room temperature for 3–5 days. The crystals were filtered, washed with toluene and 2-propanol, and dried under vacuum at room temperature.
- 2.2.3. Synthesis of AgSePy Films by the Tarnishing Method. AgSePy films were prepared by a chemical transformation reaction

- between metallic silver (Ag) and the  $Py_2Se_2$  organic precursor. The silver coated on glass substrates with the thicknesses of 15 nm were prepared by thermal evaporation with a deposition rate of  $\sim\!1.5$  Å/s. Subsequently, the obtained silver films and 30 mg of  $Py_2Se_2$  and 200  $\mu L$  of  $N_iN'$ -dimethylformamide in separate open culture tubes were sealed together inside a microwave reaction vial. After heating in an oven at 100 °C for 3 days, the silver films transformed into paleyellow AgSePy films.
- 2.2.4. Synthesis of AgSePy Powders by Ultrasonication. Small-sized AgSePy powder for thick film preparation was synthesized through ultrasonication treatment. A 30 mM solution of AgNO $_3$  in propylamine (PrNH $_2$ ) (10 mL) was added in a portion-wise manner to a 30 mM solution of Py $_2$ Se $_2$  in toluene (10 mL) at a rate of 1 mL/min under ultrasonication, using an ultrasonic probe sonicator (Vibra-Cell, VCX 750) with a time pulse of 5 s/1 s and an amplitude of 40% for 12 min. After the complete addition of AgNO $_3$ , the mixture solution was ultrasonicated for an additional 6 min. The resulting yellow solid powder of AgSePy was then centrifuged at 4500 rpm for 5 min, washed with toluene and 2-propanol, and subsequently dried under a vacuum at room temperature.
- 2.2.5. Preparation of AgSePy Thick Films. Thick AgSePy films were prepared by initially dispersing 90 mg of AgSePy powder in 1 mL of anisole. The suspension was ultrasonicated using an ultrasonic probe sonicator (Vibra-Cell, VCX 750) with a time pulse of 5 s/1 s and an amplitude of 40% for 24 min, resulting in a yellow colloidal solution. Next, 10 mg of poly(methyl methacrylate) (PMMA) was added to the AgSePy colloidal solution and immediately shaken at a rate of 500 rpm for 10 min. Following this, the mixture was heated to 100 °C for 30 min to ensure complete dissolution of the PMMA. The resulting viscous liquid (650  $\mu$ L) was then drop-cast on a 1 in. × 1 in. glass substrate treated with UV-ozone. Subsequently, the films were dried in a vacuum oven at 40 °C under a pressure of 200 mbar for 4 h. The film thickness was measured by using a Dektak® XTL stylus profilometer.
- **2.3. Characterization.** 2.3.1. Nuclear Magnetic Resonance (NMR) Spectroscopy. The <sup>1</sup>H NMR, <sup>13</sup>C NMR, and <sup>77</sup>Se NMR spectra were recorded with a Bruker 600 MHz AVANCE III HD spectrometer. The spectral data are reported as chemical shifts (in ppm) by calibrating against the peaks of the CDCl<sub>3</sub> solvent (7.26 ppm for <sup>1</sup>H NMR and 77.16 ppm for <sup>13</sup>C NMR) and Ph<sub>2</sub>Se<sub>2</sub> (463.15 ppm for <sup>77</sup>Se-NMR).
- 2.3.2. High-Resolution Mass Spectroscopy (HRMS). High-resolution mass spectra (HRMS) were acquired using a Bruker Autoflex SpeedTM mass spectrometer with an atmospheric pressure chemical ionization (APCI) source.
- 2.3.3. Thermogravimetric Analysis (TGA). TGA data was measured using a Rigaku Thermo plus EVO2 Instrument. The sample was heated from room temperature to 400  $^{\circ}$ C with a heating rate of 10  $^{\circ}$ C/min under a  $N_2$  stream (200 mL/min).
- 2.3.4. Differential Scanning Calorimetry (DSC). DSC analysis was carried out using a Mettler Toledo DSC823e instrument operated in the temperature range from 25 to 200 °C and cooled from 200 to 25 °C at a heating and cooling rate of 10 °C min<sup>-1</sup> under a nitrogen flow.
- 2.3.5. Powder X-ray Diffraction (PXRD). PXRD patterns were acquired using a Bruker D8 ADVANCE diffractometer with a bias voltage of 40 kV and a current of 40 mA using Cu K $\alpha$  radiation ( $\lambda$  = 1.5418 Å). The measurements were conducted with a step size of 0.07° and a scanning rate of 0.6°/min.
- 2.3.6. Single-Crystal X-ray Diffraction (SC-XRD). Low-temperature diffraction data were collected on Bruker-AXS X8 Kappa Duo diffractometers with  $I\mu S$  microsources using Mo K $\alpha$  radiation ( $\lambda$  = 0.71073 Å), coupled to a Photon 3 CPAD detector, performing  $\varphi$  and  $\omega$  scans. The structure of AgSePy was solved by dual-space methods using SHELXT<sup>28</sup> and refined against  $F^2$  on all data by full-matrix least-squares with SHELXL-2017<sup>29</sup> following established refinement strategies. All non-hydrogen atoms were refined anisotropically. All hydrogen atoms were included in the model at geometrically calculated positions and refined using a riding model. The isotropic displacement parameters of all hydrogen atoms were fixed to 1.2 times the U-value of the atoms they are linked to. Details of the data quality

and a summary of the residual values of the refinements are given in Table 1. Additional crystallographic information—atomic coordi-

Table 1. Crystal Data and Structure Refinement for AgSePy

	A o C o Dy
T 1 C 1	AgSePy
Empirical formula	$C_{30}H_{24}Ag_6N_6Se_6$
Formula weight	1589.53
Temperature	100(2) K
Wavelength	0.71073 Å
Crystal system	Triclinic
Space group	PĪ
Unit cell dimensions	a = $7.05880(10)$ Å, $\alpha = 114.4794(7)^{\circ}$
	$b = 12.0122(3) \text{ Å}, \beta = 101.9788(8)^{\circ}$
	$c = 12.6490(3) \text{ Å}, \gamma = 99.7187(8)^{\circ}$
Volume	914.92(3) Å <sup>3</sup>
Z	1
Density (calculated)	$2.885 \text{ Mg/m}^3$
Absorption coefficient	9.148 mm <sup>-1</sup>
F(000)	732
Crystal size	$0.170 \times 0.055 \times 0.045 \text{ mm}^3$
Theta range for data collection	1.860 to 32.577°
Index ranges	$-10 \le h \le 10, -18 \le k \le 18,$ $-19 \le l \le 19$
Reflections collected	43045
Independent reflections	6679 [R(int) = 0.0277]
Completeness to theta = $25.242^{\circ}$	100.00%
Absorption correction	Semiempirical from equivalents
Refinement method	Full-matrix least-squares on F <sup>2</sup>
Data/restraints/parameters	6679/0/217
Goodness-of-fit on F2	1.151
Final R indices [I > 2sigma(I)]	R1 = 0.0153, $wR2 = 0.0347$
R indices (all data)	R1 = 0.0168, $wR2 = 0.0351$
Extinction coefficient	n/a
Largest diff. peak and hole	0.867 and $-0.436 \text{ e}\cdot \text{Å}^{-3}$

nates, isotropic and anisotropic displacement parameters, bond lengths, and bond angles—can be found in the summary of crystallographic information in the Supporting Information (Tables S2–5).

2.3.7. UV—Vis Spectroscopy and Diffuse Reflectance Spectroscopy. Optical absorption spectra were obtained using a PerkinElmer Lambda 1050 spectrophotometer, equipped with an integrating sphere, in the transmission mode for thin film samples and the diffuse reflectance mode for solid samples.

For the diffuse reflectance mode, solid samples were prepared by grinding with dry potassium bromide (KBr) to a ~1 wt % dilution, and diffuse reflectance spectra were normalized to a 100% KBr baseline. The obtained diffuse reflectance spectra were converted into absorption spectra by the Kubelka–Munk transform:<sup>31</sup>

$$F(R) = \frac{(1-R)^2}{2R}$$

where F(R) is the Kubelka–Munk function with a value proportional to the sample's absorption coefficient, and R is the relative reflectance of the sample with the 100% KBr baseline.

2.3.8. Photoluminescence Excitation (PLE) Spectroscopy and Photoluminescence (PL) Spectroscopy. The PLE and PL spectra shown in Figure 3a were recorded with a Tecan Spark multimode plate reader. The PLE and PL spectra were measured in the excitation and emission scan modes, respectively, with emission and excitation bandwidths of 5 nm.

For other steady-state PL spectroscopy at room temperature, the measurements were conducted using an Edinburgh FLS980 spectrophotometer or a home-built microscope setup. The microscope setup consists of an inverted microscope (Nikon, Ti-U Eclipse)

equipped with a 405 nm laser diode (Picoquant, LDHDC-405M, continuous wave mode) and a cooled charge-coupled detector (Princeton Instruments, Pixis) on a spectrograph (Princeton Instruments, SP-2500).

2.3.9. Time-Resolved PL Spectroscopy. Time-resolved PL measurements were performed by using the same microscope setup as the steady-state PL measurements with some modifications. A variable repetition-rate 405 nm pulsed laser diode (Picoquant, LDHDC-405M) was used as the excitation light source. The detector used was a Si avalanche photodiode (Micro Photon Devices) connected to a counting board for time-correlated single-photon counting (PicoQuant, PicoHarp 300).

2.3.10. Temperature-Dependent PL Spectroscopy. Temperature-dependent experiments were performed by mounting samples on the coldfinger of a microscopy cryostat (Janis Research, ST-500) and flowing liquid helium through the coldfinger of the cryostat.

2.3.11. Photoluminescent Quantum Yield (PLQY). The measurement of PLQY was performed at room temperature using the absolute quantum yield method in an integrating sphere. <sup>32</sup> AgSePy samples were mounted at the center of the integrating sphere and were excited by a 405 nm laser diode (Picoquant, LDHDC-405M, continuous wave mode). The PL emission was collected by an optical fiber mounted at an exit port of the integrating sphere and directed to a fiber-optic spectrometer (Avantes).

**2.4. Density Functional Theory Calculations.** Density functional theory (DFT) calculations were performed using Quantum-ESPRESSO version  $6.8,^{33}$  employing the PBE functional and norm-conserving pseudopotential. We incorporated the DFT-D3 correction with Becke-Johnson damping to account for van der Waals interactions. A k-mesh of  $12 \times 4 \times 4$  and a kinetic energy cutoff of 70 Ry were used. The crystal structure obtained from the SC-XRD measurement was employed without any additional geometry optimization.

**2.5.** X-ray Scintillating Measurements. 2.5.1. X-ray Absorption Coefficient. The X-ray absorption coefficient was recorded using an Amptek X-ray detector (Model: XR-100T). The sample was irradiated with an area of 7.069 mm<sup>2</sup> using an X-ray generator (GE Sensing & Inspection Technologies, ISOVOLT 320 Titan E) with the tube potential range of 40–250 kV to provide a mean X-ray energy range of 33.3–207.0 keV. X-ray absorption was calculated using the following equation:

X-Ray absorption (%) = 
$$\frac{I_0 - I_s}{I_0} \times 100$$

where  $I_s$  and  $I_0$  are X-ray radiation intensity of the sample and blank, respectively.

2.5.2. Radioluminescence (RL) Measurement. The radioluminescence spectrum of the AgSePy film was measured using an Ocean Optics USB-4000, fiber-optics spectrometer. The sample was excited by an X-ray source in XRD instruments (Bruker D8 ADVANCE) with tube voltage and current of 40 kV and 40 mA, respectively. For the radiation stability test, the sample was continuously exposed to X-ray for 2 h and the RL spectra were recorded every 5 min.

2.5.3. X-ray Imaging. To capture X-ray images, AgSePy scintillator films and commercial CaWO<sub>4</sub> scintillator were exposed to X-rays at a dose rate of 1.86 mGy/s using an X-ray source (RQR-4, IEC61267 standard) with an applied voltage and current of 60 kV and 10 mA, respectively. The distance between the scintillator screen and the Xray source is 50 cm. The distances from the scintillator screen to the mirror and from the mirror to the camera are 7.6 and 6.6 cm, respectively. The X-ray images were then recorded using a Canon EOS RP digital camera with a full-frame CMOS sensor 26.2 MP, an ISO value of 25,600, and an aperture of f/6.3. A shutter speed used is 10 s/f for the AgSePy scintillator and 5 s/f for the commercial scintillator. To obtain a contrast X-ray image by a target object, a piece of lead object with number two shape and a pen were placed in front of the scintillator screen at 50 cm away from X- ray source. For the spatial resolution measurements, a standard duplex-wire type image quality identifier (IQI, KOWOTEST) was used as a target object at the same position.

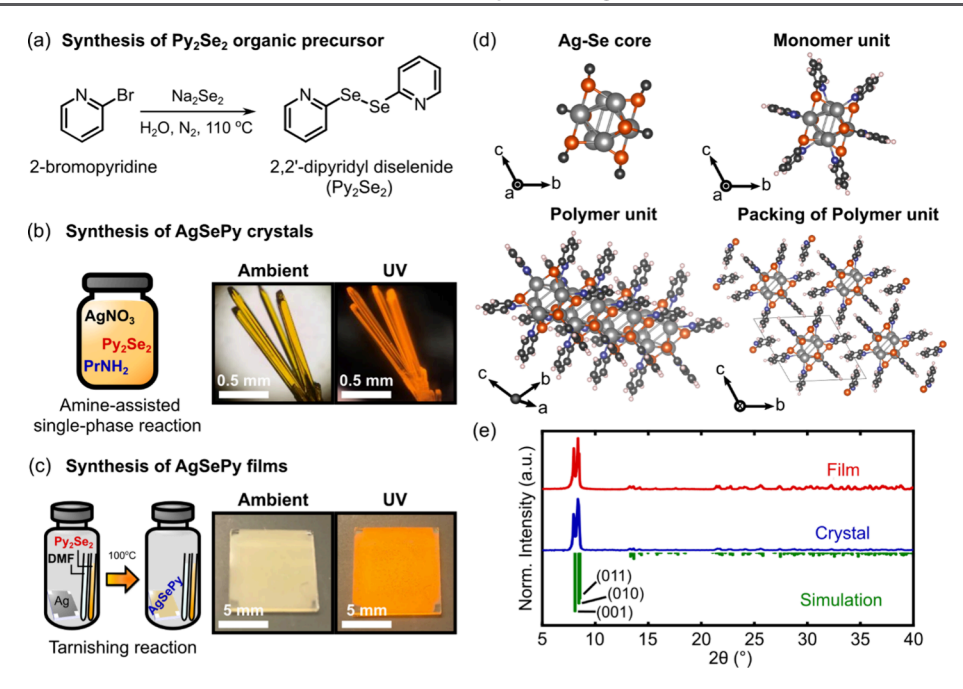


Figure 1. Preparation and Structural Characterization of AgSePy. (a) Reaction scheme to prepare Py<sub>2</sub>Se<sub>2</sub>. (b) Synthesis method and optical images of AgSePy crystals by an amine-assisted single-phase reaction. (c) Preparation and optical images of an AgSePy thin film by a tarnishing reaction. (d) Crystal structure of AgSePy. (e) PXRD patterns of AgSePy films (red) and ground crystals (blue) and their simulated pattern (green).

2.5.4. Detection Limit Measurement. The AgSePy and commercial CaWO<sub>4</sub> scintillator (Dupont Cronex DETA II UG 002814) were irradiated with an X-ray source (RQR-4, IEC61267 standard) with an applied voltage of 60 kV and the current ranging from 0.1 mA to 3.0 mA. With those conditions, the different doses of X-ray ranging from 19.41  $\mu$ Gy/s to 557.47  $\mu$ Gy/s were obtained. The pixel value of color images was obtained by measuring the mean gray value using ImageJ software. The detection limit can be achieved when the image's pixel value is three times higher than the background intensity (signal-tonoise ratio  $\sim$  3). The X-image of AgSePy and commercial scintillator with different dose rates was shown in Figure S9.

2.5.5. Light Yield Estimation. The light yield of AgSePy was estimated using a relative method as described in reference 38. The commercial CaWO<sub>4</sub> scintillator with a known light yield of 15,800 photons/MeV<sup>39</sup> was used as a reference to calculate the relative light yield of the AgSePy scintillator. To estimate the light yield, we used the equation

$$LY_{AgSePy} = LY_{CaWO4} \frac{PX_{AgSePy,normalized}}{PX_{CaWO4,normalized}}$$

where  $LY_{AgSePy}$  and  $LY_{CaWO4}$  are the light yields of our AgSePy sample and the  $CaWO_4$  scintillator (15,800 photons/MeV) and  $PX_{AgSePy,normalized}$  and  $PX_{CaWO4,normalized}$  are the normalized pixel intensity of X-ray images obtained using our AgSePy and the  $CaWO_4$  scintillator.  $PX_{normalized}$  was calculated using the equation:

$$PX_{normalized} = \frac{PX_{measured}}{\%Abs}$$

where  $PX_{measured}$  is the pixel intensity and %Abs is an X-ray absorption (%). Using the %Abs of the AgSePy and the CaWO<sub>4</sub> scintillators at 33.3 keV (Figure 1d), we estimated the light yield of the AgSePy to be 8,345 photons/MeV.

# 3. RESULT AND DISCUSSION

**3.1.** Synthesis and Structural Characterization of AgSePy. To prepare silver pyridinylselenide (AgSePy), we first synthesized an organodiselenide precursor, 2,2'-dipyridyl diselenide (Py<sub>2</sub>Se<sub>2</sub>), by a slightly modified procedure from literature. <sup>40</sup> The synthesis involved a reaction between an *in* 

situ generated sodium diselenide (Na<sub>2</sub>Se<sub>2</sub>), prepared by a reduction of selenium (Se) powders with sodium borohydride (NaBH<sub>4</sub>), and 2-bromopyridine in an aqueous medium as depicted in Figure 1a (see the Experimental Section for more information).

Following the successful synthesis of Py<sub>2</sub>Se<sub>2</sub>, AgSePy was prepared in multiple forms, including crystals and thin films. In this work, we synthesized AgSePy crystals via an amine-assisted single-phase reaction<sup>8</sup> by mixing a propylamine (PrNH<sub>2</sub>) solution of silver nitrate (AgNO<sub>3</sub>) with a toluene solution of Py<sub>2</sub>Se<sub>2</sub> in a sealed vial under dark for 3–5 days. Over time, AgSePy slowly crystallized to afford yellow millimeter-sized crystals that exhibited intense orange luminescence under ultraviolet (UV) excitation (Figure 1b).

Alternatively, we prepared AgSePy thin films based on the "tarnishing method" or the vapor-phase chemical transformation reaction between a metallic silver (Ag) film and  $Py_2Se_2.^{11,13}$  Briefly, a 15 nm-thick Ag film was deposited onto a glass substrate by thermal evaporation and was placed inside a sealed container with  $Py_2Se_2$  and  $N_{\nu}N'$ -dimethylformamide (DMF). The vial was heated at 100 °C for 3 days, transforming the metallic Ag film into a pale-yellow film of AgSePy (Figure 1c). Like the crystal samples, AgSePy thin films exhibited intense orange emission when exposed to UV light.

Due to the excellent crystallinity of the synthesized AgSePy crystals, the crystal structure of AgSePy could be obtained by single-crystal X-ray diffraction (SCXRD). AgSePy was found to crystallize in triclinic centrosymmetric space group P\overline{1} (Table 1). Figure 1d illustrates a AgSe core, a monomer unit, a polymer unit, and packing of the polymer unit of AgSePy. Each monomer unit of AgSePy consists of a hybrid organic—inorganic cluster with the formula [AgSePy]<sub>6</sub>, having a distorted octahedral Ag<sub>6</sub> core. The Ag—Ag distances in the core range from 2.92 to 3.25 Å (Figure S1a) and are comparable to the typical separations found in other reported Ag cluster complexes, 41,42 suggesting the presence of

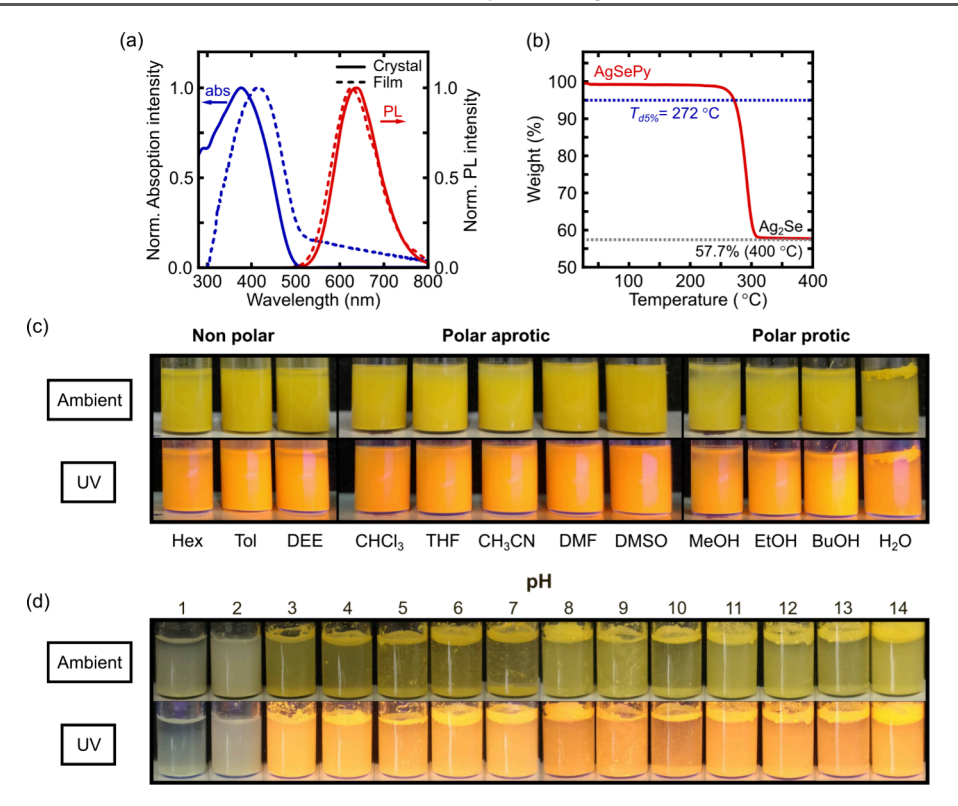


Figure 2. Optical properties and the stability of AgSePy. (a) UV–visible absorption and photoluminescence spectra of AgSePy in crystal and thin film states. (b) TGA thermogram of AgSePy. (c) Photographs of AgSePy in different solvents under ambient and UV light. The solvents tested include hexane (Hex), toluene (Tol), diethyl ether (DEE), trichloromethane (CHCl $_3$ ), tetrahydrofuran (THF), acetonitrile (CH $_3$ CN), dimethylformamide (DMF), dimethyl sulfoxide (DMSO), methanol (MeOH), ethanol (EtOH), 1-butanol (BuOH), and water (H $_2$ O). (d) Photographs of AgSePy in aqueous solution with different pH values ranging from 1 to 14.

reasonable argentophilic (Ag···Ag) interactions. The Ag<sub>6</sub> cluster core was surrounded by six organic pyridylselenide (SePy) ligands covering six out of eight faces of the octahedra. Each Ag atom is coordinated by two Se atoms and one N atom with average Ag–Se and Ag–N bond lengths of 2.59 and 2.35 Å, respectively (Figure S1b,c).

Different AgSePy monomer units are linked via the two available surfaces of each octahedron forming a one-dimensional (1D) chain (Figure S1d) and each chain is assembled into a three-dimensional (3D) structure via the van der Waals and  $\pi - \pi$  interactions of adjacent pyridine rings (Figure S1e). The closest Ag-Ag, Ag-Se, and Se-Se separations between two adjacent monomer units are 4.33, 3.70, and 3.49 Å, respectively (Figure S 1f). The Ag-Ag and Ag-Se separations are longer than the sum of their van der Waals radii of 3.44 Å<sup>43</sup> and 3.59-3.62 Å, 43 respectively, suggesting an absence of covalent bonding. However, the Se-Se separation is shorter than the sum of van der Waals radii of two Se's of 3.74-3.80 Å<sup>43</sup> but longer than the typical Se–Se bond lengths of 2.88– 2.95 Å, 44 indicating a possibility of weak covalent or strong van der Waals interaction between Se atoms. This arrangement and the possibility of intercluster Se-Se interactions of the Ag<sub>6</sub> cluster are unique compared to other previously reported Ag<sub>6</sub> clusters, which typically crystallize as discrete monomer units.41,45

Moreover, the structure of AgSePy differs from previous reports of silver organoselenide analogues, such as two-dimensional (2D) AgSePh<sup>8,26</sup> and one-dimensional (1D) AgSePh-F<sub>2</sub>(2,6) crystals, <sup>16</sup> which exhibit continuous covalent interactions between Ag and Se along their structural plane and line, respectively. This observation underscores the significance

of heteroatoms, such as the N atom on the pyridine ring, in controlling the structures of the MOCs.

To confirm the identities of AgSePy synthesized by different methods, we performed powder X-ray diffraction (PXRD) analysis on both ground crystals and thin films of AgSePy. We found that the experimentally obtained diffraction patterns matched well with the simulated PXRD pattern from the SCXRD data (Figure 1e). All PXRD patterns showed strong peaks at  $2\theta$ 's of  $7.95^{\circ}$ ,  $8.37^{\circ}$ , and  $8.46^{\circ}$ , corresponding to (001), (010), and (011) diffraction planes, respectively. Moreover, no distinct peak from other byproducts was detected including the diffraction peaks of Ag ( $\sim 38.2^{\circ}$  (111))<sup>46</sup> and Se ( $\sim 23.5^{\circ}$  (100) and  $29.7^{\circ}$  (101)),<sup>47,48</sup> suggesting excellent purity of the obtained AgSePy crystals and thin films.

3.2. Optical Properties and Stability of AgSePy. The optical absorption of AgSePy crystals and films (Figure 2a) were determined using UV-visible absorption spectroscopy in the diffuse reflectance and transmission modes, respectively. Both crystals and films each exhibited a broad absorption feature with a band edge of ~500 nm. The extracted optical band gap of AgSePy by the Kubelka-Munk function was calculated to be 2.61 eV (Figure S2). The photoluminescence (PL) spectra at room temperature of AgSePy crystals and thin films displayed broad orange photoluminescence with their emission peaks centered at 636 and 626 nm, respectively (Figure 2a), leading to a large Stoke's shift of ~259 nm. The observed large Stoke's shift in AgSePy may be attributed to its soft and deformable 0D hybrid structure, which induces a strong electron-phonon coupling effect and forms self-trapped excitons that lead to broadband light emission and large

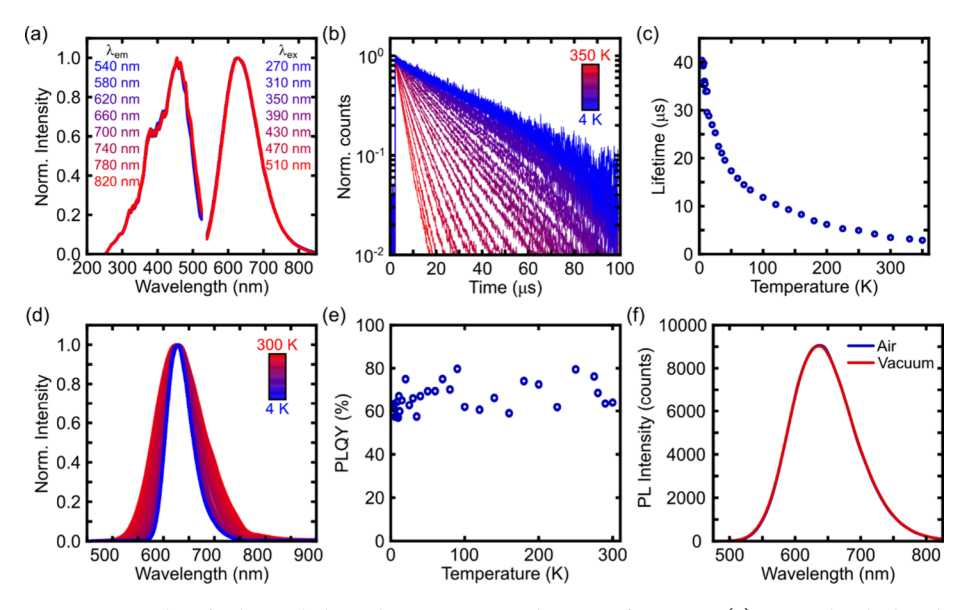


Figure 3. Optical investigations to identify the underlying luminescent mechanism of AgSePy. (a) Normalized photoluminescence excitation spectra when probed at 540–820 nm (left) and normalized photoluminescence spectra when excited with light sources at 270–510 nm (right). (b) Time-resolved photoluminescence decays of AgSePy at 4–350 K. (c) Extracted photoluminescence lifetimes of AgSePy at 4–350 K. (d) Temperature-dependent photoluminescence spectra of AgSePy obtained at 4–300 K. Temperature-dependent photoluminescence quantum yields (PLQYs) of AgSePy at 4–300 K. (f) Comparison of the photoluminescence spectra of AgSePy under air and vacuum conditions.

Stoke's shifts similar to those reported in the fields of 0D organic—inorganic hybrid metal halides and perovskites. <sup>49,50</sup> Furthermore, the slight difference in the PL spectra of these samples is likely caused by the significant difference in the sample thicknesses (~100–200 nm for films vs >0.1 mm for crystals), resulting in different degrees of light reabsorption and light out-coupling efficiency across wavelengths.

The PLQY of AgSePy was measured to be 64% under ambient conditions. This value is relatively high compared to previously reported Ag(I) clusters (Table S1), which are often nonemissive or exhibit low PLQYs. Furthermore, the PLQY of AgSePy is significantly higher than that of the prototypical member of the MOC family, silver(I) phenylselenide or AgSePh, whose PLQY is less than 2%. This difference could be attributed to the change in dimensionality from 2D to 0D, which likely increases the exciton binding energy and overlap of excited-state and ground-state wave functions.

Moreover, AgSePy showed robust thermal stability under a wide range of temperatures. Thermogravimetric analysis (TGA, Figure 2b) confirmed AgSePy's excellent thermal stability up to ~250 °C under  $\rm N_2$  with a 5% weight loss temperature ( $T_{d5\%}$ ) of 272 °C. At 400 °C, AgSePy showed a weight loss of 42.3%, corresponding to the decomposition of AgSePy to Ag<sub>2</sub>Se. Differential scanning calorimetry (DSC, Figure S3) analysis also revealed that AgSePy exhibits an exceptional phase stability, with no phase transition observed during heating and cooling scans between 25 and 200 °C.

Additionally, AgSePy exhibited a strong chemical stability against various organic solvents and pH conditions. Figure 2c reveals the insolubility and resistance of AgSePy in various common organic solvents. We found that AgSePy retained its physical appearance, original crystal phase, and strong luminescence characteristic when soaked in nonpolar (hexane, toluene, diethyl ether), polar aprotic (trichloromethane [CHCl<sub>3</sub>], tetrahydrofuran [THF], acetonitrile [CH<sub>3</sub>CN], dimethylformamide [DMF], dimethyl sulfoxide [DMSO]) and polar protic (methanol [MeOH], ethanol [EtOH], 1-

butanol [BuOH], water  $[H_2O]$ ) solvents, which was confirmed by the retention of its PXRD pattern and PLQY against various solvents (Figures S4a and S5a).

Furthermore, AgSePy was stable in aqueous solutions with pH values ranging from 3 to 14 and maintained its PXRD pattern and robust luminescence under these conditions (Figures 2d, S4b, and S5b). However, at pH below 3, yellow AgSePh transformed into a nonemissive white solid which eventually turned black. It is noteworthy that this observation differs from that of its prototypical AgSePh, which showed excellent stability under acidic conditions (Figure S6). This suggests that the acidic conditions do not interfere with the Ag—Se bonds in the core structure, and the degradation of AgSePy at the same conditions likely arises from the protonation at the pyridynyl nitrogen (N) atoms which disrupts the Ag—N bonding and the structure of AgSePy.

**3.3.** Luminescence Property of AgSePy. To investigate the luminescence property of AgSePy, we started by examining its PL properties at various photoexcitation wavelengths. Figure 3a shows the normalized photoluminescence excitation (PLE) spectra probed at 540-820 nm and the normalized PL spectra excited at 270-510 nm. Both PLE and PL spectra reveal no shift as the detection and excitation wavelengths were varied, respectively. This observation suggests that the broad PL emission of AgSePy arises from a single optical transition, which is likely the transition to the ground electronic state from the lowest singlet ( $S_1$ ) or triplet ( $T_1$ ) excited state.

Figure 3b illustrates the transient PL of AgSePy. At 300 K, the PL decay dynamics of AgSePy is well described by a single exponential function, suggesting that thermally activated delayed fluorescence (TADF) is unlikely to be the origin of its luminescence. This is in stark contrast to a similar hexanuclear Ag<sub>6</sub> complex of enantiomeric Ag<sub>6</sub>L<sub>6</sub> where L is a (S) or (R)-2-phenylglycinol ligand showing a TADF property. Moreover, the extracted PL lifetime of AgSePy was 3.4  $\mu$ s, borderline between the typical PL lifetimes of fluorescent and phosphorescent materials, <sup>52,53</sup> making it

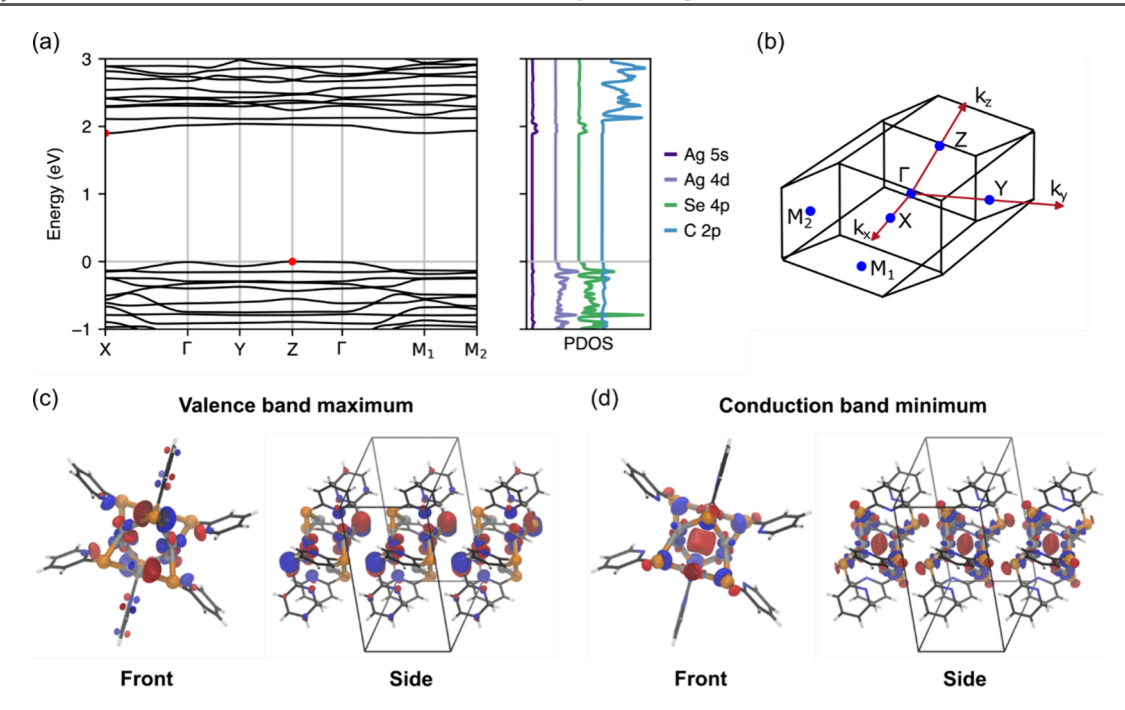


Figure 4. Calculated electronic structure of AgSePy. (a) Band structure and projected density of states of AgSePy, as calculated using DFT. The valence band maximum (VBM) and conduction band minimum (CBM) are highlighted with red circles. The energy of the VBM is set to zero, as shown by the gray horizontal line. The gray vertical lines correspond to the high-symmetry points within the first Brillouin zone. (b) The first Brillouin zone, featuring the reciprocal lattice vectors indicated by red arrows and high-symmetry k points marked with blue circles. (c, d) Wave function of VBM (c) and CBM (d). The isosurface value is set at 0.002 e/Bohr³. Blue and red surfaces represent the positive and negative phases of the wave function, respectively. Atoms are colored as follows: Ag: Gray, Se: Orange, C: Black, N: Blue, H: White.

difficult to pinpoint the luminescence mechanism from this experiment alone.

To further study the luminescence property, we then performed steady-state and transient PL spectroscopy at 4-300 K. First, we found that the PL decay dynamics of AgSePy remained single exponential throughout this temperature range (Figure 3b) and the extracted lifetime continuously increased from 3.4  $\mu$ s at 300 K to 40.4  $\mu$ s at 4 K without any sign of plateau (Figure 3c). Second, the steady-state PL spectra showed no peak shifting (Figure 3d) and the integrated PL intensity remained almost constant as the temperature was varied (Figure 3e). All these observations ascertain that the luminescent origin of AgSePy is not TADF, which normally shows a biexponential PL decay behavior, as well as a plateau in PL lifetime, a shift in PL peak position, and a significant drop in PL intensity at low temperature due to the reduced reverse intersystem crossing. 51,54,55 The peak narrowing and increasing PL lifetime at low temperature are possibly due to suppression of molecular vibration and a higher proportion of a less allowed electronic transition between the ground vibrational energy levels of the ground and excited electronic states.

Additionally, we measured the PL intensity of AgSePy under air and vacuum conditions to observe the effect of oxygen  $(O_2)$  on its luminescence property. Due to its triplet ground state,  $O_2$  is usually used to quench a  $T_1$  excited state and probe phosphorescence. Figure 3f shows the stable PL emission of AgSePy under air and vacuum conditions, indicating no quenching effect in an  $O_2$ -rich environment.

Taking all of the observations into account, we believe there are two possible luminescence mechanisms for AgSePy. The first mechanism is fluorescence, supported by the absence of quenching effect in an  $O_2$ -rich environment. While most fluorescent materials exhibit nanosecond lifetimes and small

Stokes' shifts, there are reports, particularly with lanthanide complexes,  $^{56-58}$  demonstrating microsecond lifetimes and large Stokes' shifts. The second possible mechanism is phosphorescence, indicated by the observed microsecond lifetime and large Stokes' shift of AgSePy. Although we did not detect any quenching effects in the presence of  $\rm O_2$  for AgSePy, it is worth noting that phosphorescent materials exhibiting air-stable luminescence are not uncommon and have been previously reported.  $^{59,60}$ 

3.4. Electronic Structure of AgSePy. The band structure of AgSePy was investigated by using density functional theory (DFT) calculations (Figure 4a). The valence band maximum (VBM) is located at the Z point, while the conduction band minimum (CBM) is at the X point (Figure 4a,b), giving an indirect band gap of 1.90 eV and a direct band gap of 2.03 eV at the Z point. This theoretical band gap is comparable with the experimental band gap extracted from UV-vis diffused reflectance measurement (2.61 eV). Notably, the bands exhibit minimal dispersion in all directions, suggesting limited hybridization of orbitals between neighboring monomers and confirming the 0D electronic structure of AgSePy. Such localization of charge carriers could be a contributing factor to the high PLQY of AgSePy. The wave functions of the VBM and CBM are predominantly located at the AgSe core (Figure 4c,d). Furthermore, the projected density of states indicates that the VBM of AgSePy is largely composed of Ag 4d and Se 4p orbitals, while the CBM primarily consists of Ag 5s and Se 4p orbitals. The higher conduction bands are dominated by the C 2p orbitals. The band composition is consistent with those observed in other silver organoselenides. 16,25

**3.5.** X-ray Scintillating Properties of AgSePy. The strong and stable PL properties under various temperatures and conditions along with the high-Z atomic constituent of

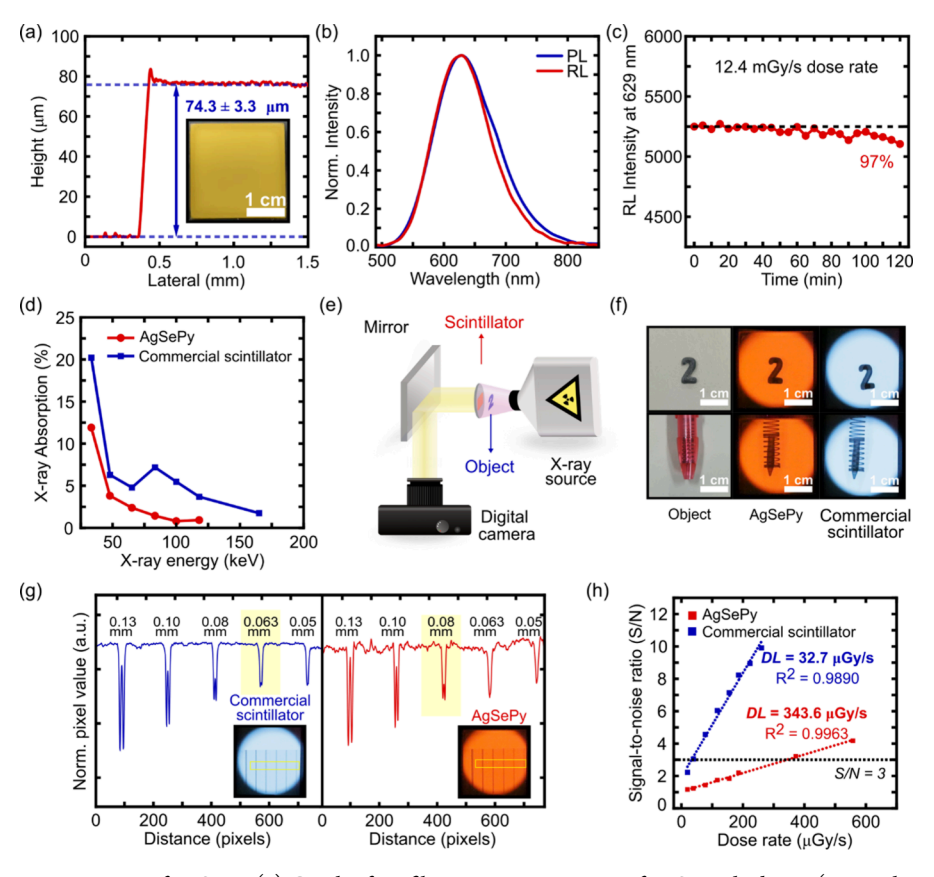


Figure 5. X-ray scintillating properties of AgSePy. (a) Graph of profilometer measurement of AgSePy thickness (inset; photograph of AgSePy thick film under ambient light). (b) Normalized photoluminescence (PL) and X-ray radioluminescence (RL) spectra of AgSePy. (c) The RL stability of AgSePy under continuous X-ray radiation at a dose rate of 12.4 mGy/s. (d) X-ray absorption spectra of AgSePy and a commercial CaWO<sub>4</sub> scintillator (Dupont Cronex DETA II UG 002814). (e) A schematic diagram of the X-ray imaging setup. (f) X-ray images of the lead object and pen obtained using AgSePy and the commercial CaWO<sub>4</sub> scintillator screen. (g) Spatial resolution plots of AgSePy and the commercial CaWO<sub>4</sub> scintillator screen. Yellow regions indicate the smallest details that the films can resolve, and all X-ray images were recorded under the same dose rate of 1.86 mGy s<sup>-1</sup>. (h) The linear relationship of the RL signal response of AgSePy and the commercial CaWO<sub>4</sub> scintillator as a function of X-ray dose, along with the detection limits determined at signal-to-noise ratio (S/N) of 3.

AgSePy are attractive characteristics for X-ray detection applications. To test the possible use of AgSePy as an X-ray scintillator, we first prepared a thick AgSePy film on a glass substrate by drop-casting a colloidal solution of AgSePy (an average particle size of 916.1  $\pm$  42.1 nm, Figure S7) in anisole with an added polymer binder, poly(methyl methacrylate) (PMMA). The smooth AgSePy film (Figure 5a) with a thickness of 74.3  $\pm$  3.3  $\mu m$  was obtained by using a mixed solution of 90 mg of AgSePy and 10 mg of PMMA in 1 mL of anisole.

Under excitation with X-rays, this AgSePy film exhibited an orange radioluminescence (RL) centered at 629 nm, which is consistent with its PL spectrum (Figure 5b), indicating a common luminescence mechanism. Compared to the emission of a commercial CaWO $_4$  scintillator film (Dupont Cronex DETA II UG 002814), the AgSePy's light yield was estimated to be  $\sim$ 8,000 photons/MeV (see Experimental Section for the calculation method). Moreover, its RL intensity was maintained up to 97% under continuous exposure of X-rays at 12.4 mGy/s for 2 h (Figure 5c). This result suggests a high radiation stability of the material, which is one of the crucial requirements of a good scintillator candidate.  $^{61}$ 

To compare the scintillating performance of AgSePy with that of the commercial CaWO<sub>4</sub> film, we then performed the X-ray absorption ability of both scintillator films in the mean X-

ray energy ranges of 33.3–207.0 keV (Figure 5d). The absorption coefficient of the AgSePy scintillator showed a good X-ray absorption ability on the same order as the commercial CaWO<sub>4</sub> films, indicating a good comparability between these two scintillation samples.

Next, we performed an X-ray imaging experiment using a custom-built setup (Figure 5e). In this setup, X-ray radiation was directed to a target object positioned in front of a scintillator film, and the scintillator film's luminescence was reflected by a mirror into a digital camera. Figure 5f shows images of a number-two-shaped lead object and a pen that we used as our test targets along with the corresponding X-ray photographs obtained by our AgSePy film and a commercial CaWO<sub>4</sub> scintillator film. The resulting photograph from the AgSePy film shows a good contrast and allows inner structure inspection of the pen with a metallic spring and a ballpoint head inside its plastic body with the quality on par with the result from the commercial CaWO<sub>4</sub> scintillator film.

Resolving power or spatial resolution is an important characteristic of a good X-ray scintillator film. To determine the spatial resolution, we performed an X-ray imaging experiment using a standard duplex-wire type image quality identifier (IQI) as a target object (Figures 5g and S8). This IQI consists of a series of two parallel lines with separations ranging from 0.800 to 0.032 mm. Using this IQI, we found that

our AgSePy film shows a remarkable resolving power down to 0.080  $\pm$  0.005 mm. This is almost on par with the spatial resolution of the commercial CaWO<sub>4</sub> film, which has the resolving power of 0.063  $\pm$  0.005 mm.

Another crucial attribute of an excellent X-ray scintillator film is its detection limit. This is conventionally identified by the X-ray dose rate that gives the signal-to-noise (S/N) ratio of 3.<sup>62,63</sup> By varying the X-ray dose rates (Figures 5h and S9) using the same setup, we determined the detection limits of our AgSePy film and the commercial scintillator film to be 343.6  $\mu$ Gy s<sup>-1</sup> and 32.7  $\mu$ Gy s<sup>-1</sup>, respectively. While both values exceed the medical diagnostic requirement of 5.5  $\mu$ Gy/s, it is important to note that these values are sensitive to the detector's capability and can be improved by employing a more sensitive optical sensor. Therefore, we recommend readers to interpret the detection limit of AgSePy in comparison to that of the commercial reference, rather than relying solely on absolute terms. Additionally, we found that the RL intensity of the AgSePy film showed a linear relationship with the X-ray dose rate, which is another important requirement in practical applications of scintillator materials. 62,64

As an X-ray absorption coefficient ( $\mu$ ) is described by  $\mu \propto \rho Z^4$  where Z is the atomic number and  $\rho$  is the density of material, <sup>65</sup> we believe there is a big space for improving the performance of AgSePy and MOC scintillators. For example, the removal of the polymer binder and the introduction of heavier atoms into MOC structures via organic modification and metal substitution/alloying are potential directions in increasing the  $\rho$  and Z concentration to ultimately improve the overall scintillating properties of this novel class of materials.

## 4. CONCLUSION

In summary, AgSePy bearing a pyridine ligand was successfully prepared as single crystals and thin films by the amine-assisted crystallization and the tarnishing method. While the prototypical AgSePh crystallizes as a 2D semiconductor, replacing the phenyl group with the pyridinyl group of an organic ligand causes a structural change from 2D sheets to a 0D complex via the formation of Ag-N coordination bonds. The optical properties of AgSePy exhibited a 0D hybrid characteristic including broadband orange emission ( $\lambda_{\rm em} \sim 636$  nm), large Stokes shifts ( $\sim$ 259 nm), long lifetime (3.4  $\mu$ s), and high PLQY (64%). Further optical investigations by PLE spectroscopy and steady-state and time-resolved PL spectroscopy at varying temperatures and conditions suggest fluorescence and phosphorescence as two possible mechanisms governing its optical properties. Additionally, AgSePy showed excellent thermal and chemical stability due to its covalent bonding nature, distinguishing it from other X-ray scintillating materials such as traditional metal halide salts and perovskites, which are unstable in air and humid conditions. 66,67 The combined merits of regulated heavy-metal-free, chemical robustness, high PLQY, and negligible self-absorption along with the high-Z atomic constituent of AgSePy result in promising X-ray scintillation performance with an estimated light yield of  $\sim$ 8,000 phe/MeV and a resolving power down to 0.080  $\pm$ 0.005 mm. This study is an early report of MOCs as an X-ray scintillator, showcasing the impact of molecular designs and opening new uses of MOCs in radiation detection and X-ray imaging.

#### ASSOCIATED CONTENT

## Supporting Information

The Supporting Information is available free of charge at https://pubs.acs.org/doi/10.1021/acs.chemmater.4c00653.

Additional structural figures and X-ray scintillating properties of AgSePy, nuclear magnetic resonance and mass spectra of  $Py_2Se_2$ , summary of previously reported Ag(I) clusters, and additional crystallographic information on AgSePy (PDF)

X-ray crystallographic information on AgSePy (CIF)

### **Accession Codes**

CCDC-2324702 contains the supplementary crystallographic data for this paper. These data can be obtained free of charge via <a href="https://www.ccdc.cam.ac.uk/data\_request/cif">www.ccdc.cam.ac.uk/data\_request/cif</a>, or by emailing data\_request@ccdc.cam.ac.uk, or by contacting The Cambridge Crystallographic Data Centre, 12 Union Road, Cambridge CB2 1EZ, UK; fax: + 44 1223 336033.

## AUTHOR INFORMATION

## **Corresponding Authors**

Watcharaphol Paritmongkol — Department of Materials Science and Engineering, School of Molecular Science and Engineering, Vidyasirimedhi Institute of Science and Technology, Rayong 21210, Thailand; Department of Chemical Engineering, Massachusetts Institute of Technology, Cambridge, Massachusetts 02139, United States;
orcid.org/0000-0003-1638-6828;

Email: watcharaphol.p@vistec.ac.th

William A. Tisdale — Department of Chemical Engineering, Massachusetts Institute of Technology, Cambridge, Massachusetts 02139, United States; oorcid.org/0000-0002-6615-5342; Email: tisdale@mit.edu

#### **Authors**

Rattapon Khamlue — Department of Materials Science and Engineering, School of Molecular Science and Engineering, Vidyasirimedhi Institute of Science and Technology, Rayong 21210, Thailand; orcid.org/0009-0007-1733-8437

Tomoaki Sakurada — Department of Chemical Engineering, Massachusetts Institute of Technology, Cambridge, Massachusetts 02139, United States; orcid.org/0000-0002-2353-7324

Yeongsu Cho – Department of Chemical Engineering, Massachusetts Institute of Technology, Cambridge, Massachusetts 02139, United States

Woo Seok Lee – Department of Chemical Engineering, Massachusetts Institute of Technology, Cambridge, Massachusetts 02139, United States; Department of Materials Science and Engineering, Massachusetts Institute of Technology, Cambridge, Massachusetts 02139, United States; orcid.org/0000-0001-9188-5104

Pimpan Leangtanom – Department of Materials Science and Engineering, School of Molecular Science and Engineering, Vidyasirimedhi Institute of Science and Technology, Rayong 21210, Thailand; orcid.org/0009-0001-8421-3980

Michael G. Taylor — Department of Chemical Engineering, Massachusetts Institute of Technology, Cambridge, Massachusetts 02139, United States; orcid.org/0000-0003-4327-2746

Worakit Naewthong — Photonics Technology Research Team, National Electronics and Computer Technology Center,

- Pathum Thani 12120, Thailand; o orcid.org/0009-0001-6221-320X
- Pongsakun Sripetch Photonics Technology Research Team, National Electronics and Computer Technology Center, Pathum Thani 12120, Thailand
- Busayakorn Na Ranong Thailand Institute of Nuclear Technology (Public Organization), Nakorn Nayok 26120,, Thailand
- Tossawat Autila Thailand Institute of Nuclear Technology (Public Organization), Nakorn Nayok 26120,, Thailand
- Thiti Rungseesumran Thailand Institute of Nuclear Technology (Public Organization), Nakorn Nayok 26120,, Thailand
- Jakrapong Kaewkhao Center of Excellence in Glass Technology and Materials Science (CEGM), Nakhon Pathom Rajabhat University, Nakhon Pathom 73000, Thailand
- Taweesak Sudyoadsuk Department of Materials Science and Engineering, School of Molecular Science and Engineering, Vidyasirimedhi Institute of Science and Technology, Rayong 21210, Thailand
- Atcha Kopwitthaya Photonics Technology Research Team, National Electronics and Computer Technology Center, Pathum Thani 12120, Thailand; occid.org/0000-0002-6544-0512
- Peter Müller Department of Chemistry, Massachusetts Institute of Technology, Cambridge, Massachusetts 02139, United States; oorcid.org/0000-0001-6530-3852
- Vinich Promarak Department of Materials Science and Engineering, School of Molecular Science and Engineering, Vidyasirimedhi Institute of Science and Technology, Rayong 21210, Thailand; ⊚ orcid.org/0000-0003-4805-9944
- Heather J. Kulik Department of Chemical Engineering, Massachusetts Institute of Technology, Cambridge, Massachusetts 02139, United States; Department of Chemistry, Massachusetts Institute of Technology, Cambridge, Massachusetts 02139, United States; orcid.org/0000-0001-9342-0191

Complete contact information is available at: https://pubs.acs.org/10.1021/acs.chemmater.4c00653

# **Author Contributions**

VR.K. and T.S. contributed equally to this paper.

#### Notes

The authors declare no competing financial interest.

### ACKNOWLEDGMENTS

Synthesis, structural refinement, and spectroscopic characterization at MIT was supported by the U.S. Army Research Office under Award Number W911NF-23-1-0229. Synthesis, characterization, and investigation of X-ray scintillating properties at VISTEC were supported by National Science Research Foundation via the Program Management Unit for Human Resources & Institutional Development, Research and Innovation under Award Number B50G670105, National Research Council of Thailand (NRCT) Research Grant for New Scholar under Award Number N42A670121, and Vidyasirimedhi Institute of Science and Technology (VISTEC) Start-Up Grant for New Faculty Member. This work made use of the MRSEC Shared Experimental Facilities at MIT, supported by the National Science Foundation under award number DMR-08-19762. DFT calculations were

supported by the United States Department of Energy under grant number DE-NA0003965 (Y.C.) and DE-SC0024174 (H.J.K.). R.K. and P.L. were supported by a VISTEC scholarship. T.S. was supported by AGC Inc. (former Asahi Glass Co., Ltd.). W.S.L was partially supported by the Seoul Broadcasting System Foundation Overseas Doctoral Program Scholarship.

#### ■ REFERENCES

- (1) Veselska, O.; Demessence, A. d10 coinage metal organic chalcogenolates: From oligomers to coordination polymers. *Coord. Chem. Rev.* **2018**, 355, 240–270.
- (2) Yan, H.; Hohman, J. N.; Li, F. H.; Jia, C.; Solis-Ibarra, D.; Wu, B.; Dahl, J. E.; Carlson, R. M.; Tkachenko, B. A.; Fokin, A. A.; et al. Hybrid metal-organic chalcogenide nanowires with electrically conductive inorganic core through diamondoid-directed assembly. *Nature materials* **2017**, *16* (3), 349–355.
- (3) Rabl, H.; Myakala, S. N.; Rath, J.; Fickl, B.; Schubert, J. S.; Apaydin, D. H.; Eder, D. Microwave-assisted synthesis of metalorganic chalcogenolate assemblies as electrocatalysts for syngas production. *Communications Chemistry* **2023**, *6* (1), 43.
- (4) Jiang, H.; Cao, L.; Li, Y.; Li, W.; Ye, X.; Deng, W.; Jiang, X.; Wang, G.; Xu, G. Organic "receptor" fully covered few-layer organic-metal chalcogenides for high-performance chemiresistive gas sensing at room temperature. *Chem. Commun.* **2020**, *56* (40), 5366–5369.
- (5) Okhrimenko, L.; Cibaka Ndaya, C.; Fateeva, A.; Ledoux, G.; Demessence, A. Post-synthetic functionalization and ligand exchange reactions in gold (i) phenylthiolate-based coordination polymers. *New J. Chem.* **2020**, *44* (41), 17970–17975.
- (6) Popple, D. C.; Schriber, E. A.; Yeung, M.; Hohman, J. N. Competing Roles of Crystallization and Degradation of a Metal-Organic Chalcogenolate Assembly under Biphasic Solvothermal Conditions. *Langmuir* **2018**, *34* (47), 14265–14273.
- (7) Schriber, E. A.; Rosenberg, D. J.; Kelly, R. P.; Ghodsi, A.; Hohman, J. N. Investigation of Nucleation and Growth at a Liquid-Liquid Interface by Solvent Exchange and Synchrotron Small-Angle X-Ray Scattering. Frontiers in Chemistry 2021, 9, 593637.
- (8) Paritmongkol, W.; Sakurada, T.; Lee, W. S.; Wan, R.; Muller, P.; Tisdale, W. A. Size and quality enhancement of 2D semiconducting metal-organic chalcogenolates by amine addition. *J. Am. Chem. Soc.* **2021**, *143* (48), 20256–20263.
- (9) Cuthbert, H. L.; Wallbank, A. I.; Taylor, N. J.; Corrigan, J. F. Synthesis and Structural Characterization of [Cu20Se4 (μ3-SePh) 12 (PPh3) 6] and [Ag (SePh)]∞. Zeitschrift für anorganische und allgemeine Chemie 2002, 628 (11), 2483–2488.
- (10) Fratelli, I.; Maserati, L.; Basirico, L.; Galeazzi, A.; Passarella, B.; Ciavatti, A.; Caironi, M.; Fraboni, B. Layered metal-organic chalcogenide thin films for flexible and largearea X-ray direct detection. *Frontiers in Physics* **2023**, DOI: 10.3389/fphy.2023.1325164.
- (11) Paritmongkol, W.; Lee, W. S.; Shcherbakov-Wu, W.; Ha, S. K.; Sakurada, T.; Oh, S. J.; Tisdale, W. A. Morphological control of 2D hybrid organic-inorganic semiconductor AgSePh. *ACS Nano* **2022**, *16* (2), 2054–2065.
- (12) Maserati, L.; Prato, M.; Pecorario, S.; Passarella, B.; Perinot, A.; Thomas, A. A.; Melloni, F.; Natali, D.; Caironi, M. Photo-electrical properties of 2D quantum confined metal-organic chalcogenide nanocrystal films. *Nanoscale* **2021**, *13* (1), 233–241.
- (13) Trang, B.; Yeung, M.; Popple, D. C.; Schriber, E. A.; Brady, M. A.; Kuykendall, T. R.; Hohman, J. N. Tarnishing silver metal into mithrene. J. Am. Chem. Soc. 2018, 140 (42), 13892–13903.
- (14) Yeung, M.; Popple, D. C.; Schriber, E. A.; Teat, S. J.; Beavers, C. M.; Demessence, A.; Kuykendall, T. R.; Hohman, J. N. Corrosion of Late-and Post-Transition Metals into Metal-Organic Chalcogenolates and Implications for Nanodevice Architectures. ACS Applied Nano Materials 2020, 3 (4), 3568–3577.
- (15) Yang, H.; Mandal, S.; Lee, Y. H.; Park, J. Y.; Zhao, H.; Yuan, C.; Huang, L.; Chen, M.; Dou, L. Dimensionality Engineering of Lead

- Organic Chalcogenide Semiconductors. *J. Am. Chem. Soc.* **2023**, 145 (44), 23963–23971.
- (16) Sakurada, T.; Cho, Y.; Paritmongkol, W.; Lee, W. S.; Wan, R.; Su, A.; Shcherbakov-Wu, W.; Müller, P.; Kulik, H. J.; Tisdale, W. A. 1D Hybrid Semiconductor Silver 2, 6-Difluorophenylselenolate. *J. Am. Chem. Soc.* **2023**, *145* (9), 5183–5190.
- (17) Li, Y.; Jiang, X.; Fu, Z.; Huang, Q.; Wang, G.-E.; Deng, W.-H.; Wang, C.; Li, Z.; Yin, W.; Chen, B.; et al. Coordination assembly of 2D ordered organic metal chalcogenides with widely tunable electronic band gaps. *Nat. Commun.* **2020**, *11* (1), 261.
- (18) Troyano, J.; Castillo, O.; Martínez, J. I.; Fernández-Moreira, V.; Ballesteros, Y.; Maspoch, D.; Zamora, F.; Delgado, S. Reversible Thermochromic Polymeric Thin Films Made of Ultrathin 2D Crystals of Coordination Polymers Based on Copper (I)-Thiophenolates. *Adv. Funct. Mater.* **2018**, 28 (5), 1704040.
- (19) Yao, K.; Collins, M. S.; Nell, K. M.; Barnard, E. S.; Borys, N. J.; Kuykendall, T.; Hohman, J. N.; Schuck, P. J. Strongly quantum-confined blue-emitting excitons in chemically configurable multi-quantum wells. *ACS Nano* **2021**, *15* (3), 4085–4092.
- (20) Vaidya, S.; Veselska, O.; Zhadan, A.; Diaz-Lopez, M.; Joly, Y.; Bordet, P.; Guillou, N.; Dujardin, C.; Ledoux, G.; Toche, F.; et al. Transparent and luminescent glasses of gold thiolate coordination polymers. *Chemical Science* **2020**, *11* (26), 6815–6823.
- (21) Hernandez Oendra, A. C.; Aspect, M. A.; Jaeggi, J. L.; Baumann, J.; Lightner, C. R.; Pun, A. B.; Norris, D. J. Tunable Synthesis of Metal-Organic Chalcogenide Semiconductor Nanocrystals. *Chem. Mater.* **2023**, *35* (21), 9390–9398.
- (22) Veselska, O.; Dessal, C.; Melizi, S.; Guillou, N.; Podbevšek, D.; Ledoux, G.; Elkaim, E.; Fateeva, A.; Demessence, A. New Lamellar Silver Thiolate Coordination Polymers with Tunable Photoluminescence Energies by Metal Substitution. *Inorg. Chem.* **2019**, *58* (1), 99–105.
- (23) Veselska, O.; Vaidya, S.; Das, C.; Guillou, N.; Bordet, P.; Fateeva, A.; Toche, F.; Chiriac, R.; Ledoux, G.; Wuttke, S. Cyclic Solid-State Multiple Phase Changes with Tuned Photoemission in a Gold Thiolate Coordination Polymer. *Angew. Chem., Int. Ed.* **2022**, *61* (14), No. e202117261.
- (24) Maserati, L.; Refaely-Abramson, S.; Kastl, C.; Chen, C. T.; Borys, N. J.; Eisler, C. N.; Collins, M. S.; Smidt, T. E.; Barnard, E. S.; Schriber, E. A. Anisotropic 2D excitons unveiled in organic-inorganic quantum wells. *Materials horizons* **2021**, 8 (1), 197–208.
- (25) Lee, W. S.; Cho, Y.; Powers, E. R.; Paritmongkol, W.; Sakurada, T.; Kulik, H. J.; Tisdale, W. A. Light Emission in 2D Silver Phenylchalcogenolates. *ACS Nano* **2022**, *16* (12), 20318–20328.
- (26) Schriber, E. A.; Popple, D. C.; Yeung, M.; Brady, M. A.; Corlett, S. A.; Hohman, J. N. Mithrene is a self-assembling robustly blue luminescent metal-organic chalcogenolate assembly for 2D optoelectronic applications. *ACS Applied Nano Materials* **2018**, *1* (7), 3498–3508
- (27) Wang, G. E.; Luo, S.; Di, T.; Fu, Z.; Xu, G. Layered Organic Metal Chalcogenides (OMCs): From Bulk to Two-Dimensional Materials. *Angew. Chem., Int. Ed.* **2022**, *61* (27), No. e202203151.
- (28) Sheldrick, G. M. SHELXT Integrated space-group and crystal-structure determination. *Acta Crystallogr., Sect. A: Found. Adv.* **2015**, 71 (1), 3–8.
- (29) Sheldrick, G. M. Crystal structure refinement with SHELXL. Acta Crystallogr., Sect. C: Struct. Chem. 2015, 71 (1), 3-8.
- (30) Müller, P. Practical suggestions for better crystal structures. Crystallography Reviews **2009**, 15 (1), 57–83.
- (31) Kubelka, P.; Munk, F. An article on optics of paint layers. *Z. Technol. Phys.* **1931**, *12* (593-601), 259–274.
- (32) de Mello, J. C.; Wittmann, H. F.; Friend, R. H. An improved experimental determination of external photoluminescence quantum efficiency. *Advanced materials* **1997**, *9* (3), 230–232.
- (33) Giannozzi, P.; Baroni, S.; Bonini, N.; Calandra, M.; Car, R.; Cavazzoni, C.; Ceresoli, D.; Chiarotti, G. L.; Cococcioni, M.; Dabo, I.; et al. QUANTUM ESPRESSO: a modular and open-source software project for quantum simulations of materials. *J. Phys.: Condens. Matter* **2009**, *21* (39), 395502.

- (34) Perdew, J. P.; Burke, K.; Ernzerhof, M. Generalized gradient approximation made simple. *Physical review letters* **1996**, 77 (18), 3865
- (35) Hamann, D. Optimized norm-conserving Vanderbilt pseudopotentials. *Phys. Rev. B* **2013**, *88* (8), 085117.
- (36) Grimme, S.; Antony, J.; Ehrlich, S.; Krieg, H. A consistent and accurate ab initio parametrization of density functional dispersion correction (DFT-D) for the 94 elements H-Pu. *J. Chem. Phys.* **2010**, 132 (15), 154104.
- (37) Grimme, S.; Ehrlich, S.; Goerigk, L. Effect of the damping function in dispersion corrected density functional theory. *Journal of computational chemistry* **2011**, 32 (7), 1456–1465.
- (38) Ma, W.; Jiang, T.; Yang, Z.; Zhang, H.; Su, Y.; Chen, Z.; Chen, X.; Ma, Y.; Zhu, W.; Yu, X.; et al. Highly Resolved and Robust Dynamic X-Ray Imaging Using Perovskite Glass-Ceramic Scintillator with Reduced Light Scattering. *Advanced Science* **2021**, 8 (15), 2003728.
- (39) Moszyński, M.; Balcerzyk, M.; Czarnacki, W.; Nassalski, A.; Szczęśniak, T.; Kraus, H.; Mikhailik, V.; Solskii, I. Characterization of CaWO4 scintillator at room and liquid nitrogen temperatures. *Nuclear Instruments and Methods in Physics Research Section A: Accelerators, Spectrometers, Detectors and Associated Equipment* **2005**, 553 (3), 578–591.
- (40) Hodage, A. S.; Parashiva Prabhu, C.; Phadnis, P. P.; Wadawale, A.; Priyadarsini, K. I.; Jain, V. K. Synthesis, characterization, structures and GPx mimicking activity of pyridyl and pyrimidyl based organoselenium compounds. *J. Organomet. Chem.* **2012**, *720*, 19–25.
- (41) Pérez-Lourido, P. A.; García-Vázquez, J. A.; Romero, J.; Louro, M. S.; Sousa, A.; Chen, Q.; Chang, Y.; Zubieta, J. Electrochemical synthesis and crystal structure of silver (I) complexes with some heterocyclic thiones. *J. Chem. Soc., Dalton Trans.* 1996, No. 10, 2047–2054
- (42) Wu, Y.; Wu, X.; Fang, S.; Yang, S.; Li, W.; Wang, H.; Yu, X. A novel hexanuclear silver (I) complex with photoluminescence properties. *Polyhedron* **2017**, *122*, 155–160.
- (43) Bondi, A. v. van der Waals volumes and radii. *J. Phys. Chem.* **1964**, *68* (3), 441–451.
- (44) Zhang, S.; Wang, X.; Su, Y.; Qiu, Y.; Zhang, Z.; Wang, X. Isolation and reversible dimerization of a selenium-selenium three-electron  $\sigma$ -bond. *Nat. Commun.* **2014**, S (1), 4127.
- (45) Karmakar, G.; Tyagi, A.; Shah, A. Y.; Nigam, S.; Wadawale, A.; Kedarnath, G.; Vats, B. G.; Naveen Kumar, N.; Singh, V. Facile one pot synthesis of highly photoresponsive coinage metal selenides (Cu 1.8 Se and Ag 2 Se) achieved through novel Cu and Ag pyridylselenolates as molecular precursors. *Dalton Transactions* 2022, 51 (33), 12670–12685.
- (46) Alharthi, F. A.; Alghamdi, A. A.; Al-Zaqri, N.; Alanazi, H. S.; Alsyahi, A. A.; Marghany, A. E.; Ahmad, N. Facile one-pot green synthesis of Ag-ZnO Nanocomposites using potato peeland their Ag concentration dependent photocatalytic properties. *Sci. Rep.* **2020**, *10* (1), 20229.
- (47) Jiang, F.; Cai, W.; Tan, G. Facile synthesis and optical properties of small selenium nanocrystals and nanorods. *Nanoscale Res. Lett.* **2017**, *12*, 401.
- (48) Ruiz Fresneda, M. A.; Delgado Martín, J.; Gómez Bolívar, J.; Fernández Cantos, M. V.; Bosch-Estévez, G.; Martínez Moreno, M. F.; Merroun, M. L. Green synthesis and biotransformation of amorphous Se nanospheres to trigonal 1D Se nanostructures: impact on Se mobility within the concept of radioactive waste disposal. *Environmental Science: Nano* **2018**, 5 (9), 2103–2116.
- (49) Li, D.-Y.; Shang, Y.-B.; Liu, Q.; Zhang, H.-W.; Zhang, X.-Y.; Yue, C.-Y.; Lei, X.-W. 0D hybrid indium halide as a highly efficient X-ray scintillation and ultra-sensitive fluorescent probe. *Materials Horizons* **2023**, *10* (11), 5004–5015.
- (50) Wang, Z.; Wu, D.; Huang, Q.; Guo, L.; Wang, Y.; Chen, W.; Wang, F.; Du, J.; Liu, Z.; Hu, Z.; et al. Tellurium-Doped 0D Organic-Inorganic Hybrid Lead-Free Perovskite for X-ray Imaging. *Inorg. Chem.* **2023**, 62 (46), 19006–19014.

- (51) Han, Z.; Dong, X.-Y.; Luo, P.; Li, S.; Wang, Z.-Y.; Zang, S.-Q.; Mak, T. C. Ultrastable atomically precise chiral silver clusters with more than 95% quantum efficiency. *Science Advances* **2020**, *6* (6), No. eaay0107.
- (52) Valeur, B.; Berberan-Santos, M. N. Molecular fluorescence: principles and applications; John Wiley & Sons: 2012.
- (53) Shi, H.; Yao, W.; Ye, W.; Ma, H.; Huang, W.; An, Z. Ultralong Organic Phosphorescence: From Material Design to Applications. *Acc. Chem. Res.* **2022**, *55* (23), 3445–3459.
- (54) Wu, T.-L.; Huang, M.-J.; Lin, C.-C.; Huang, P.-Y.; Chou, T.-Y.; Chen-Cheng, R.-W.; Lin, H.-W.; Liu, R.-S.; Cheng, C.-H. Diboron compound-based organic light-emitting diodes with high efficiency and reduced efficiency roll-off. *Nat. Photonics* **2018**, *12* (4), 235–240.
- (55) Uoyama, H.; Goushi, K.; Shizu, K.; Nomura, H.; Adachi, C. Highly efficient organic light-emitting diodes from delayed fluorescence. *Nature* **2012**, 492 (7428), 234–238.
- (56) Aita, K.; Temma, T.; Kuge, Y.; Saji, H. Development of a novel neodymium compound for in vivo fluorescence imaging. *Luminescence: The journal of biological and chemical luminescence* **2007**, 22 (5), 455–461.
- (57) Leif, R. C.; Vallarino, L. M.; Becker, M. C.; Yang, S. Increasing the luminescence of lanthanide complexes. *Cytometry Part A: The Journal of the International Society for Analytical Cytology* **2006**, *69A* (8), 767–778.
- (58) Eliseeva, S. V.; Bünzli, J.-C. G. Lanthanide luminescence for functional materials and bio-sciences. *Chem. Soc. Rev.* **2010**, 39 (1), 189–227.
- (59) Li, K.; Wan, Q.; Yang, C.; Chang, X. Y.; Low, K. H.; Che, C. M. Air-Stable Blue Phosphorescent Tetradentate Platinum (II) Complexes as Strong Photo-Reductant. *Angew. Chem.* **2018**, *130* (43), 14325–14329.
- (60) Imoto, H.; Tanaka, S.; Kato, T.; Watase, S.; Matsukawa, K.; Yumura, T.; Naka, K. Highly efficient solid-state phosphorescence of platinum dihalide complexes with 9-Phenyl-9-arsafluorene ligands. *Organometallics* **2016**, 35 (3), 364–369.
- (61) Huang, R.-W.; Song, X.; Chen, S.; Yin, J.; Maity, P.; Wang, J.; Shao, B.; Zhu, H.; Dong, C.; Yuan, P.; et al. Radioluminescent Cu-Au Metal Nanoclusters: Synthesis and Self-Assembly for Efficient X-ray Scintillation and Imaging. *J. Am. Chem. Soc.* **2023**, *145* (25), 13816–13827.
- (62) Niu, X.; Xiao, J.; Lou, B.; Yan, Z.; Zhou, Q.; Lin, T.; Ma, C.; Han, X. Highly efficient blue emissive copper halide Cs5Cu3Cl6I2 scintillators for X-ray detection and imaging. *Ceram. Int.* **2022**, 48 (20), 30788–30796.
- (63) Xu, L.-J.; Lin, X.; He, Q.; Worku, M.; Ma, B. Highly efficient eco-friendly X-ray scintillators based on an organic manganese halide. *Nat. Commun.* **2020**, *11* (1), 4329.
- (64) Yuan, P.; He, T.; Zhou, Y.; Yin, J.; Zhang, H.; Zhang, Y.; Yuan, X.; Dong, C.; Huang, R.; Shao, W.; et al. Hybrid Thermally Activated Nanocluster Fluorophores for X-ray Scintillators. *ACS Energy Letters* **2023**, *8*, 5088–5097.
- (65) Wang, X.; Shi, H.; Ma, H.; Ye, W.; Song, L.; Zan, J.; Yao, X.; Ou, X.; Yang, G.; Zhao, Z.; et al. Organic phosphors with bright triplet excitons for efficient X-ray-excited luminescence. *Nat. Photonics* **2021**, *15* (3), 187–192.
- (66) Vaněček, V.; Děcká, K.; Mihóková, E.; Čuba, V.; Král, R.; Nikl, M.; et al. Advanced halide scintillators: From the bulk to nano. Advanced Photonics Research 2022, 3 (8), 2200011.
- (67) Lu, L.; Sun, M.; Wu, T.; Lu, Q.; Chen, B.; Huang, B. Allinorganic perovskite nanocrystals: next-generation scintillation materials for high-resolution X-ray imaging. *Nanoscale Advances* **2022**, *4* (3), 680–696.